Chapter 30
Evolution on the Main Sequence

30.1 Change in the Hydrogen Content

In the main-sequence phase, the large energy losses from a star's surface are compensated by the energy production of hydrogen burning (see Sect. 18.5.1). These reactions release nuclear binding energy by converting hydrogen into helium. This chemical evolution of the star concerns primarily its central region, since the energy sources are strongly concentrated towards the centre (Sect. 22.2).

Somewhat larger volumes are affected simultaneously if there is a convective core in which the turbulent motions provide a very effective mixing. If the extent of convective regions and the rate of energy production ε_{H} for all mass elements are known, the rate of change of the hydrogen content X_{H} can be calculated according to Sect. 8.2.3.

The situation is particularly simple for stars of rather small mass (say $0.1 M_{\odot} < M \lesssim 1 M_{\odot}$) that have a radiative core. In the absence of mixing, the change of X_{H} at any given mass element is proportional to the local value of ε_{H}. After a small time step Δt, the change of hydrogen concentration is $\Delta X_{\mathrm{H}} \sim \varepsilon_{\mathrm{H}} \Delta t$ everywhere (with a well-known factor of proportionality). Following the chemical evolution in this way over many consecutive time steps, one obtains "hydrogen profiles" [i.e. functions $X_{\mathrm{H}}(m)$] as shown in Fig. 30.1. At the end of the main-sequence phase, $X_{\mathrm{H}} \to 0$ in the centre.

With the change in the hydrogen profile also a change in the energy generation rate ε_{H} takes place (Fig. 30.2). Initially, it has a maximum at the centre, since there temperature is highest and the abundance of hydrogen almost the same everywhere in the core. However, in the course of evolution, though temperature rises in the centre, the hydrogen abundance drops, and after some time, the maximum ε_{H}, which depends on both of these quantities, is larger outside the centre. This can be seen first for the model of 8.2×10^9 years (dotted line in Fig. 30.2). When the centre is completely depleted of hydrogen, $\varepsilon_{\mathrm{H}} = 0$ there and the energy generation profile looks like the strongly peaked (solid) line, corresponding to the final model of Fig. 30.1. Energy is now being produced effectively in a shell around the exhausted

R. Kippenhahn et al., *Stellar Structure and Evolution*, Astronomy and Astrophysics Library, DOI 10.1007/978-3-642-30304-3_30, © Springer-Verlag Berlin Heidelberg 2012

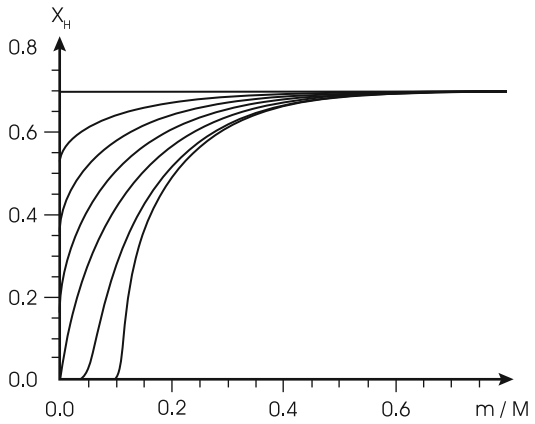

Fig. 30.1 Hydrogen profiles showing the gradual exhaustion of hydrogen in a star of $1M_\odot$. The homogeneous initial model consists of a mixture with $X_\mathrm{H} = 0.700$ and $X_\mathrm{He} = 0.280$. The hydrogen content X_H over m/M is plotted for seven models which correspond to an age of 0.0, 2.2, 4.2, 6.2, 8.2, 10.2, and 11.2×10^9 years after the onset of hydrogen burning

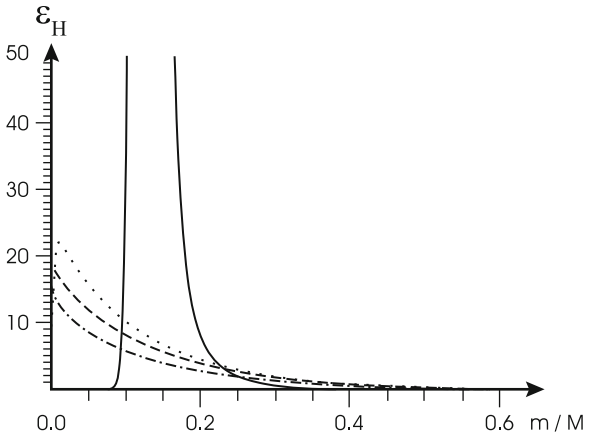

Fig. 30.2 Profiles of nuclear energy production ε_H from hydrogen burning (in erg/gs) for some of the models for which hydrogen profiles are shown in Fig. 30.1. These are the ones at the very beginning of hydrogen burning (*dash-dotted line*) and at ages of 6.2 (*dashed*), 8.2 (*dotted*), and 11.2×10^9 years (*solid line*). The maximum energy generation rate in this latter model is 170 erg/gs

core. This "hydrogen-shell burning" is taking place within the much larger region, in which core hydrogen burning has reduced the hydrogen content. It leads to a steepening of that profile and to a narrowing of the burning shell. Hydrogen burning is now even for this $1\ M_\odot$ star proceeding via the CNO cycle.

In more massive stars, the helium production is even more concentrated towards the centre because of the large sensitivity to temperature of the CNO cycle. But the mixing inside the central convective core is so rapid compared to the local production of new nuclei that the core is virtually homogeneous at any time. Inside the core, $\Delta X_\mathrm{H} \sim \bar{\varepsilon}_\mathrm{H} \Delta t$ with an energy production rate $\bar{\varepsilon}_\mathrm{H}$ averaged over the whole core. The only difficulty comes from the fact that the border of the convective core may change during the time step Δt. The numerical calculations show that for stars below $10M_\odot$ the mass M_c of the convective core decreases with progressive hydrogen consumption, which leads to a hydrogen profile $X_\mathrm{H}(m)$, as shown in Fig. 30.3 for a $5\,M_\odot$ star. At the end of central hydrogen burning, one has a helium core with $M_\mathrm{He} \approx 0.1M$, and the envelope in which X_H still

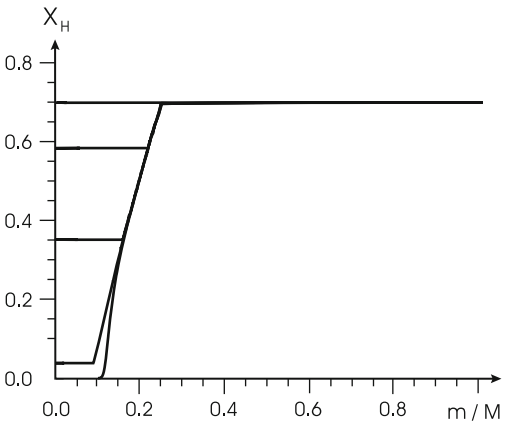

Fig. 30.3 The hydrogen profile $X_H(m)$ that is established in a 5 $M_\odot$ star of the same composition as in Fig. 30.1 during and at the end of hydrogen burning in a shrinking convective core. With decreasing central hydrogen content the age of the models is 0.7, 23, 55, 78, and 82×10^6 years

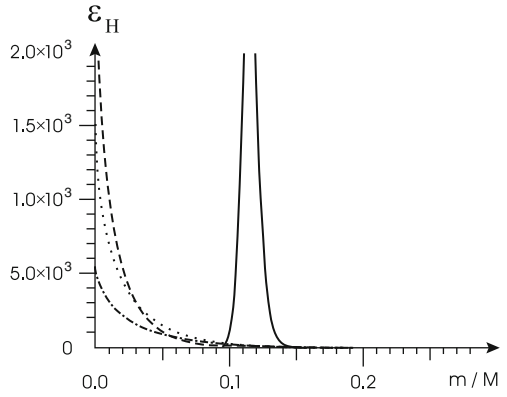

Fig. 30.4 Energy production profiles for the models with an age of 0.7 (*dash-dotted*), 55 (*dotted*), 78 (*dashed*), and 82×10^6 years (*solid line*) of Fig. 30.3. ε_H, the energy generation rate by hydrogen burning (in units of erg/gs), is about 10^4 times larger than in the 1 $M_\odot$ star (Fig. 30.2) and has a maximum of 2.6×10^4 erg/gs in the last model

has almost its original value. The corresponding energy production is shown in Fig. 30.4. Notice that it is more and more concentrated towards the centre with progressing main-sequence evolution and that the energy producing shell is located just outside the helium core left after the end of central hydrogen burning. Similar hydrogen and energy production profiles are established in stars with other values of M. The main difference is that with increasing M the hydrogen profile is gradually shifted to larger values of m/M, i.e. the relative mass of the produced helium core increases with M. The corresponding increase of the convective core with increasing M for zero-age main-sequence (ZAMS) models has already been shown in Fig. 22.7.

This simple scenario is seriously complicated, particularly for rather massive stars, by two uncertainties in the theory of convection (convective overshoot and semiconvection). These effects will be dealt with separately in Sect. 30.4.

30.2 Evolution in the Hertzsprung–Russell Diagram

At the beginning of the main-sequence phase the models are located in the HR diagram on or near the ZAMS as described in Chap. 22. Numerical solutions show that their positions change relatively little during the long phase in which hydrogen is exhausted in the central region. A typical evolutionary track (for a $7M_\odot$ star of the same population I mixture as before) is given in Fig. 30.5a. Starting from point A on the ZAMS, the luminosity increases by about $\Delta \lg L = 0.240$ to point B and about $\Delta \lg L = 0.059$ from B to C. The rise of L is due to the increasing mean molecular weight when ^{1}H is transformed to ^{4}He, in accordance with the prediction of the homology relations [see, e.g. (20.20)]. The evolution from B to C is so fast that μ increases only a very little in this short time interval. From the change of r for different values of m (see Fig. 31.3) one clearly sees that the star evolves non-homologously, which ultimately is because the chemical composition changes only in the central region. The solutions show that the effective temperature decreases from A to B by $\Delta \lg T_{\rm eff} \approx -0.089$ and then increases again to point C by $\Delta \lg T_{\rm eff} \approx 0.038$. This corresponds to an increase of the radius by $\Delta \lg R \approx 0.299$ (A to B) and a decrease by $\Delta \lg R \approx 0.047$ (B to C). Point B is reached after about 3.67×10^7 years, roughly when the central hydrogen content has dropped to $X_{\rm H} \approx 0.05$. At point C, when $X_{\rm H} = 0$ in the centre, the age is 3.74×10^7 years.

The evolutionary tracks are very similar for all stellar masses for which the hydrogen content is exhausted in a convective core of appreciable mass, i.e. on the whole upper part of the main sequence (see Fig. 30.5b). The increments of $\lg L$ from A to B and from A to C become somewhat larger for larger values of M, while the changes of $\lg T_{\rm eff}$ remain about the same. The structure of the evolutionary tracks is different for smaller masses which have radiative cores. This can be seen in the lower part of Fig. 30.5b. Of particular interest is the star with $M = 1.2\,M_\odot$, since it barely develops a convective core of only $0.05\,M_\odot$. This is also visible in the shape of its track in the Hertzsprung–Russell diagram, which appears to be a transition between those for lower and higher masses.

A common feature of all evolutionary tracks described here is that they point in some direction *above* the ZAMS. This is the case only for an evolution producing chemically inhomogeneous models (composed of a helium core and a hydrogen-rich envelope). In an evolution assuming complete mixing of the whole model, μ would have a constant spatial distribution and would increase in time. Then the star would evolve below the ZAMS, in accordance with the discussion after (20.23). Aside from all details, the observations (e.g. cluster diagrams) show that evolved stars are in fact above and to the right of the ZAMS, i.e. the stars obviously develop chemical inhomogeneities in their interior. This conclusion is very important, in particular, for the theory of stellar rotation. It excludes, for example, a complete mixing by the large-scale currents of rotationally driven meridional circulations (Chap. 44).

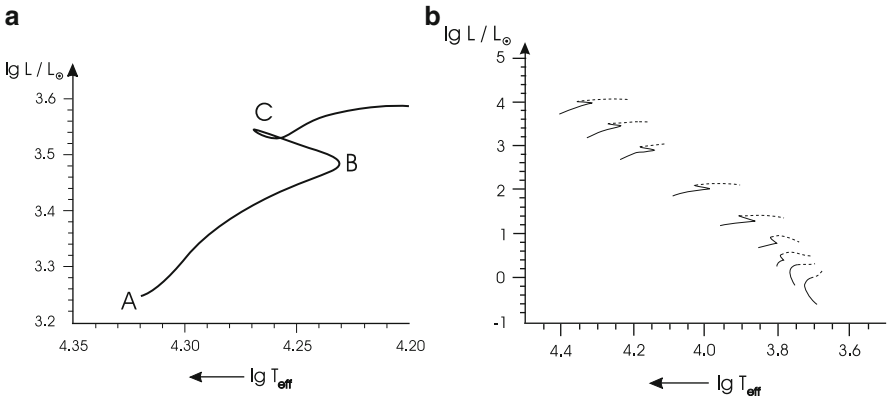

Fig. 30.5 Hertzsprung–Russell diagrams with evolutionary tracks for population I stars during central hydrogen burning (main-sequence phase). The tracks start on the zero-age main-sequence and extend into the post-main-sequence phase. (**a**) For stellar mass $M = 7M_{\odot}$. Some characteristic models are labelled by A (age zero), B (minimum of $T_{\rm eff}$), and C (exhaustion of central hydrogen). (**b**) For stellar masses $M = 0.8$, 1.0, 1.2, 1.5, 2.0, 3.0, 5.0, 7.0, and $10\,M_{\odot}$. The *dotted parts* of the tracks indicate their continuation into the ensuing phase after central hydrogen exhaustion

30.3 Timescales for Central Hydrogen Burning

The time $\tau_{\rm H}$ a star spends on the main sequence while burning its central hydrogen depends on M. This is because its luminosity L increases so strongly with M. Let us consider this timescale:

$$\tau_{\rm H} = \frac{E_{\rm H}}{L}, \tag{30.1}$$

where $E_{\rm H}$ is the nuclear energy content that can be released by central hydrogen burning. As a rough estimate, we assume that the same fraction of the total mass of hydrogen $M_{\rm H}$ in the star is consumed in all stars. Then we have $E_{\rm H} \sim M_{\rm H} \sim M$. Since L does not vary very much in this phase, we take the M–L relation of the ZAMS, $L \sim M^{\eta}$ [cf. (22.1)]. Introducing these proportionalities into (30.1), we have for the dependence of $\tau_{\rm H}$ on M

$$\tau_{\rm H}(M) \sim \frac{M}{L} \sim M^{1-\eta}. \tag{30.2}$$

For an average exponent in the M–L relation of, say, $\eta = 3.5$, one has $\tau_{\rm H} \sim M^{-2.5}$, i.e. a strong decrease of $\tau_{\rm H}$ towards larger values of M.

Of course, the numerical results are influenced and modified by a variety of details. The sequence of calculations made for Fig. 30.5b yields $\tau_{\rm H}/(10^6\,\text{years}) =$ 23,283.89, 2,420.24, 303.32, 37.42, and 18.91 for $M/M_{\odot} = 0.8$, 1.5, 3.0, 7.0, and 10, respectively. In all the cases with a convective core, by far the largest part of $\tau_{\rm H}$

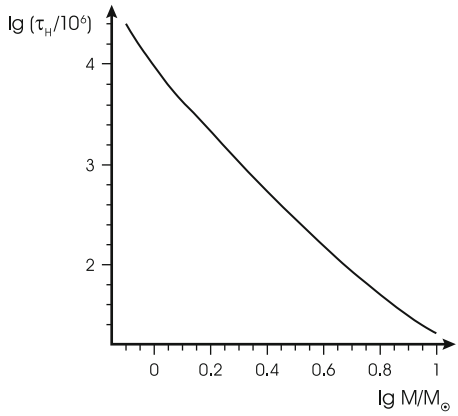

Fig. 30.6. Hydrogen-burning times against stellar mass obtained from the calculations done for Fig. 30.5b

is spent in the first phase between points A and B, while the last part (B–C) covers only about 3 %...5 %. Figure 30.6 shows the main-sequence lifetime as function of mass in a double-logarithmic plot. The mean slope is ≈ -2.8, corresponding to $\eta \approx 3.8$.

Although the absolute values are very uncertain (Sect. 30.4), the general trend is clear and has remarkable consequences for the observed HR diagrams of star clusters, by which it is confirmed. Assume that all stars of such a cluster were formed at the same time, i.e. that they now have the same age τ_{cluster}. We must then conclude that all stars with masses larger than a limiting mass M_0 have already left the main-sequence region, while stars with $M < M_0$ are still on the main sequence. M_0 is given by the condition $\tau_{\text{cluster}} = \tau_{\text{H}}(M_0)$. This is the basis for the age determination of such clusters.

30.4 Complications Connected with Convection

The seemingly nice and clear picture of the main-sequence phase as described above is unfortunately blurred by the notorious problem of convection. Questionable points include the precise determination of those regions in the deep interior in which convective motions occur and therefore the extent to which the chemical elements are mixed. The mixing influences the later evolution, since the chemical profile, which is established and left behind, is a long-lasting memory. We briefly mention two problems, the first of which concerns all main-sequence stars having convective cores, while the second occurs only in the more massive of these stars.

30.4.1 Convective Overshooting

We consider the situation in the surroundings of the outer boundary of a convective core of mass $M_{\rm bc}$, as calculated without allowance for overshooting. This means that here we have defined the boundary to be at the position of neutral stability, i.e. where

$$\nabla_{\rm rad} = \nabla_{\rm ad} \tag{30.3}$$

according to the classical criterion (6.13). (Without much loss of generality, we may here treat a chemically homogeneous layer, for example, in the model for a ZAMS star.) Complete mixing and a nearly adiabatic stratification with $\nabla = \nabla_{\rm ad} + \varepsilon (0 < \varepsilon \ll 1)$ is assumed in the convective region below $M_{\rm bc}$, while no mixing and $\nabla = \nabla_{\rm rad}$ is assumed for the radiative region above $M_{\rm bc}$ (cf. Chaps. 6 and 7, in particular Sect. 7.3).

This model implies an obvious problem: the boundary between the regimes in which convective motions are present ($v > 0$) and absent ($v = 0$) is determined by the criterion (30.3), which essentially relies on buoyancy forces, and therefore describes the *acceleration* $\dot{v}$ rather than the velocity v (cf. Sect. 6.1). Rising elements of convection are accelerated until they have reached $M_{\rm bc}$; the braking starts only beyond this border, which is passed by elements owing to their inertia. The situation is the same as if we were to hope that a car would come to a full stop at the very point where one switches from acceleration to braking. The only way to substantiate this would be to try it (once) right in front of a hard and solid enough wall.

Simple estimates (e.g. Saslaw and Schwarzschild 1965) indeed give the impression that there is such a hard wall for elements passing the border $M_{\rm bc}$. We have seen in Sect. 7.4 that in the deep interior of the star the elements rise adiabatically such that $\nabla_{\rm e} = \nabla_{\rm ad}$. From (7.5) we then see that the buoyancy force k_r acting on an element is

$$k_r \sim \nabla - \nabla_{\rm ad} \,, \tag{30.4}$$

with a positive factor of proportionality. Below the border, k_r is small and positive (small acceleration) since $\nabla - \nabla_{\rm ad}$ is extremely small and positive ($\approx 10^{-6}$). In contrast to this, the braking *above* the border is by orders of magnitude more efficient. We have assumed that there ∇ is equal to $\nabla_{\rm rad}$, which drops rapidly below $\nabla_{\rm ad}$ (in Fig. 22.8b by about 0.1 within a scale height). So the force k_r due to $\nabla - \nabla_{\rm ad}$ soon reaches rather large and negative values: therefore an overshooting element can be stopped within a negligible fraction of the pressure scale height.

A significant overshoot, therefore, could result only if the braking were substantially reduced (the "wall" softened). A possibility for this was outlined by Shaviv and Salpeter (1973), who pointed to the recoupling of the overshoot on the thermal structure of the layer. Consider the temperature excess DT of a moving element ($\nabla_{\rm e} = \nabla_{\rm ad}$) over the surroundings (gradient ∇). According to (7.4), we have $DT \sim \nabla - \nabla_{\rm ad}$, and DT becomes negative above the border, i.e. the overshooting elements become cooler than the surroundings, which results in a cooling of the

upper layers and an increase of the gradient ∇. We may describe it in terms of the convective flux (positive, if it points outwards), which according to (7.3) is

$$F_{\rm con} \sim v \cdot DT \tag{30.5}$$

(with positive factors of proportionality). Above the border, the upward motion ($v > 0$) of cooler elements ($DT < 0$) represents a negative $F_{\rm con}$. In order to maintain a constant total flux

$$F = F_{\rm con} + F_{\rm rad} = \frac{l}{4\pi r^2}, \tag{30.6}$$

with $F_{\rm con} < 0$, the radiative flux $F_{\rm rad}$ must become larger than the total flux F. From (7.1) and (7.2) we immediately have

$$\frac{F_{\rm rad}}{F} = \frac{\nabla}{\nabla_{\rm rad}}\,, \tag{30.7}$$

which shows that $\nabla > \nabla_{\rm rad}$ for $F_{\rm rad} > F$. The increase of ∇, however, reduces the absolute values of $\nabla - \nabla_{\rm ad}$ and of the braking force k_r compared with the situation without overshooting; the elements can penetrate farther into the region of stability than originally estimated, etc.

To find out whether or not this provides an appreciable amount of overshooting is a difficult problem and one that is still far from being solved. In order to find the point where the velocity v vanishes, one needs a self-consistent and detailed solution (including velocities, fluxes, gradients) for the whole convective core. This can only be obtained by using a theory of convection, the uncertainties of which now enter directly into the interior solution of the star. Even if we want to apply the mixing-length theory, the procedure is not clear. Instead of the usual local version of the theory, one needs a non-local treatment. At a given point, for example, the velocity of an element or its temperature excess depends not only on quantities at that point, but on the precise amount of acceleration (and braking) which the element has experienced along its whole previous path. All prescriptions for evaluating this and for averaging quantities like v or DT are as arbitrary as the choice of the mixing length. In fact any detailed modelling of the convective core by a mixing-length theory is necessarily ambiguous. For example, it encounters the difficulty that a core extends over less than a pressure scale height [the local expression of which, $H_P = -dr/d\ln P$, becomes ∞ at the centre according to (11.7)]. Different authors using different prescriptions have arrived at answers ranging from virtually no overshoot to rather extensive overshoot; and all of them have been questioned (see Renzini 1987). In the following we present a physically motivated treatment by Maeder (1975). Figure 30.7 shows the typical run of some characteristic functions as obtained from such calculations for $M = 2M_\odot$ and $\alpha = \ell_{\rm m}/H_P = 1$. Below the "classical" border of stability ($\nabla_{\rm rad} = \nabla_{\rm ad}$), one has typically $\nabla - \nabla_{\rm ad} \approx +10^{-4}$ which is enough to accelerate the convective elements

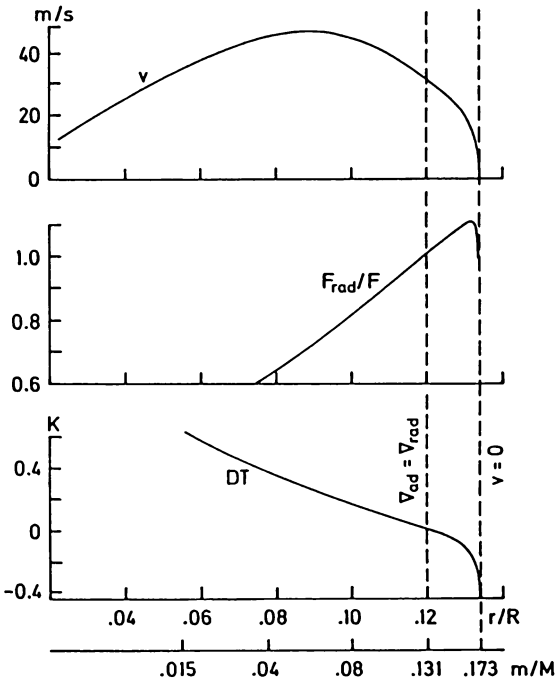

Fig. 30.7. Velocity v and temperature excess DT of rising convective elements and the ratio of the radiative flux $F_{\rm rad}$ relative to the total flux F around the border of stability ($\nabla_{\rm rad} = \nabla_{\rm ad}$) in a star of $2M_\odot$. Overshooting calculated with $\alpha = \ell_{\rm m}/H_P = 1$ extends to the point where $v = 0$ (after Maeder 1975)

to $30 \cdots 40\,\mathrm{ms}^{-1}$. Above the border, where still $v > 0$, but $DT < 0$, $F_{\rm rad}$ exceeds the total flux F by about 10 %, while $\nabla - \nabla_{\rm ad}$ ranges from -10^{-4} to -10^{-2}. The overshooting reaches to the point with $v = 0$, which occurs at about 14 % of the local scale height H_P above the border, corresponding to an increase of the mass of the convective core $M_{\rm c}$ of more than 30 %. This amount depends on the assumed value of α, because the velocity of the convective elements depends on the mixing length $\ell_{\rm m}$ according to (7.6). Figure 30.8a shows the hydrogen profile established during hydrogen burning in a $7M_\odot$ star calculated with such overshooting for different α (The limit case $\alpha = 0$ is the model calculated without overshooting.). The influence of overshooting on the evolutionary tracks is shown in Fig. 30.8b. The consequences of an increased helium core at the end of this phase are an increased luminosity, an increased age (by about 25 % for $\alpha = 1$) due to the enlarged reservoir of nuclear fuel, and lower effective temperatures reached during the main-sequence evolution. This leads to a broadening of the upper main-sequence compared to calculations without overshooting. Indeed, the observed width of the upper main-sequence is one test to estimate the amount of overshooting from convective cores in massive stars (Maeder and Meynet 1991). However, if such overshooting occurs, its main effect will show up only later, during the phase of helium burning (see Sect. 31.4).

As mentioned at the beginning of Chap. 7 efforts to develop more realistic convection models, based on either the Reynolds stress approach or on multi-dimensional simulations, have been made. Such models would be non-local by

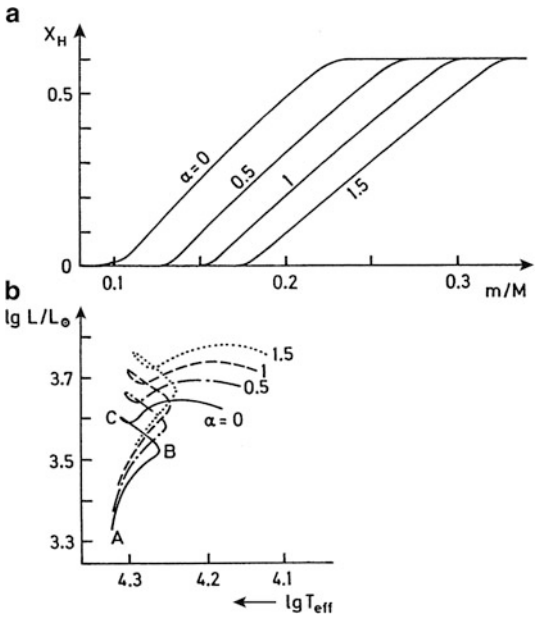

Fig. 30.8. Central hydrogen burning for a $7M_\odot$ star (initial mixture $X_\mathrm{H} = 0.602$, $X_\mathrm{rest} = 0.044$) with overshooting according to different assumptions for the ratio $\alpha = \ell_\mathrm{m}/H_P$ ($\alpha = 0$ means no overshooting). (**a**) The hydrogen profile at the end of this phase. (**b**) HR diagram with evolutionary tracks (Matraka et al. 1982)

nature and therefore include the necessary conditions for treating also overshooting more realistically.

Up to the present time two standard methods for modelling overshooting are being used in numerical calculations. The first one is based on a simple extension of the convectively mixed region above the boundary defined by the Schwarzschild criterion. This extension l_ov is parametrized in terms of the local pressure scale height at the boundary

$$l_\mathrm{ov} = \alpha_\mathrm{ov} H_P \,. \tag{30.8}$$

The parameter α_ov is typically of order $0.1 \cdots 0.2$ for modern stellar models. It has no relation to the mixing-length parameter α_MLT, and is most often determined by fitting models to observed colour-magnitude diagrams (e.g. Stothers and Chin 1992). For the overshooting region the assumption $\nabla = \nabla_\mathrm{ad}$ is usually made. One sometimes speaks of "convective penetration" instead of overshooting. Strictly speaking, the temperature gradient should be at least slightly subadiabatic, otherwise convective elements would not be decelerated.

In an alternative approach, convective overshooting is considered to be a diffusive process with a diffusion constant

$$D(z) = D_0 \exp \frac{-2z}{f_\mathrm{ov} H_P}, \tag{30.9}$$

where z is the radial distance from the formal Schwarzschild border and f_ov the free parameter of this description. D_0 sets the scale of diffusive speed and is

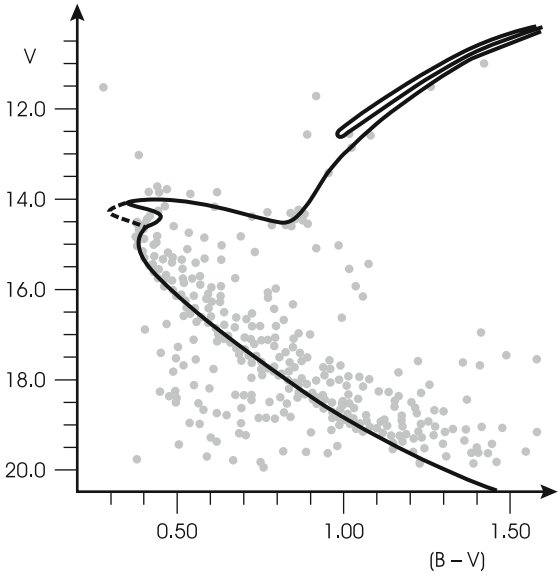

Fig. 30.9. Fit of isochrones to the colour-magnitude diagram of the open cluster NGC 2420 (adopted from Pietrinferni et al. 2004). The *dashed line* is obtained from stellar models without overshooting, and the *solid line* for models with overshooting, treated in the approach of (30.8), with a parameter $\alpha_{\rm ov}$ of about 0.1. The "hook" at the end of the main-sequence can be reproduced correctly only with overshooting taken into account. Note that the isochrone age is 3.2 Gyr for this case, while it is lower (2 Gyr) for the case without overshooting to balance the fact that in this case main sequence luminosities are lower. Except for the turn-off region the two isochrones are almost identical

derived from the convective velocity obtained from mixing-length theory and taken below the Schwarzschild boundary. This approach is based on two-dimensional hydrodynamical simulations of thin convective envelopes in A-type stars and cool white dwarfs. Although its theoretical foundation is therefore limited, it has been used in a variety of situations and been shown that it also can be used to reproduce the width of the upper main sequence, and the colour-magnitude diagrams of open clusters (Fig. 30.9), with a numerical value of $f_{\rm ov}$ in the range of 0.02. The hydrodynamical models also indicate that the temperature gradient in the overshooting layers is close to the radiative one. A further advantage of this approach is that it can easily be added to a stellar evolution code that already has implemented diffusion (Sect. 8.2.2). In both cases the extent of the overshooting region has to be limited for small convective cores because of the divergence of H_P near the centre, as one otherwise gets unrealistically large mixed cores.

The "diffusive" approach (30.9) leads to smoother chemical profiles than those resulting from (30.8). This is quite obvious from the example we show in Fig. 30.10 for a star of $15 M_\odot$. The solid black lines are for the calculation without overshooting taken into account. The receding convective core leaves behind a profile

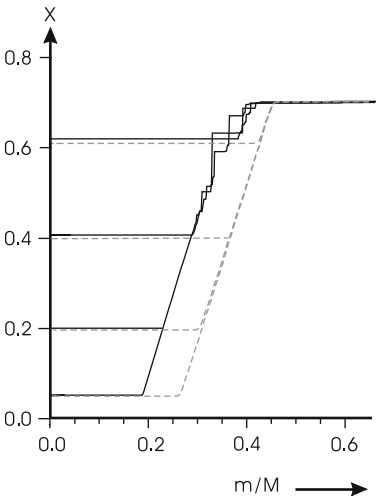

Fig. 30.10. Hydrogen profiles in a $15M_\odot$ star during the main-sequence evolution. The *solid black lines* refer to a model without, the *dashed grey lines* to one with overshooting being included. Four models at approximately the same central hydrogen content, but not necessarily the same age, are being compared

characterized by small steps mixed with shallow, homogeneously mixed regions, which have been unstable to convection locally. In Fig. 30.12 this kind of structure shows up as "convective tongues" in the upper panel. The dashed grey lines are the resulting chemical profiles if overshooting according to (30.9) is included. Due to the exponentially declining mixing speed the profiles are very smooth. It is also clearly seen how overshooting extends the homogeneously mixed core by about $0.05M$ in this case. For a large part of the main-sequence evolution the Schwarzschild boundary of the convective core remains at about the same mass coordinate as in the case without overshooting. Only in later main-sequence phases it changes (see Fig. 30.12, top and middle panel).

But as mentioned before the question of overshooting is quite open and can be settled only by use of a better theory of convection. This also concerns the question how the amount of overshooting varies with stellar parameters, such as mass and composition, and whether it occurs at all convective boundaries. So far, both issues can be addressed only tentatively by comparison with observations.

30.4.2 Semiconvection

Another phenomenon related to convection introduces a large amount of uncertainty in the evolution of rather massive stars, say, for $M > 10M_\odot$ (This limit depends on the chemical composition; it can even be around $7M_\odot$ for hydrogen-rich mixtures of extreme population I stars.).

In these stars during central hydrogen burning the convective core retreats, leaving a certain hydrogen profile behind; the radiative gradient $\nabla_{\rm rad}$ outside the core starts to rise and soon exceeds the adiabatic gradient $\nabla_{\rm ad}$. This happens in a

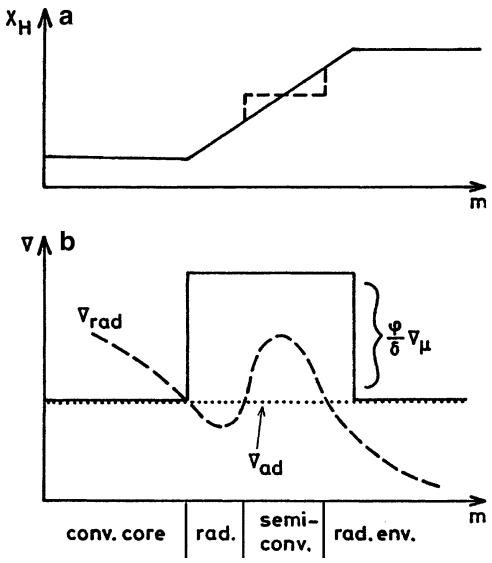

Fig. 30.11. Schematic illustration of the example for semiconvection discussed in the text. The *solid line* in (**a**) shows a hydrogen profile in which semiconvection occurs. Complete mixing in this layer would lead to the *dashed* "plateau". The gradients in the same range of m are sketched in (**b**), indicating the radiative-semiconvective-convective properties of the different layers

region with outwardly increasing hydrogen content (decreasing molecular weight μ); therefore $\nabla_\mu \equiv d \ln \mu / d \ln P > 0$, which makes the layer dynamically stable (Sect. 6.1). Considering the classical criteria for convective stability according to Schwarzschild and Ledoux we find

$$\nabla_{ad} < \nabla_{rad} < \nabla_{ad} + \frac{\varphi}{\delta}\nabla_\mu . \tag{30.10}$$

As described in Sect. 6.3 a layer in which (30.10) is fulfilled is vibrationally unstable ("overstable"). A slightly displaced mass element starts to oscillate with slowly growing amplitude and penetrates more and more into regions of different chemical composition. This results in a rather slow mixing which is called *semiconvection.* The treatment of this process is complicated, one difficulty being that any degree of mixing must have a noticeable reaction on the stratification in the mixed layer.

Suppose that semiconvection occurs in some region of an originally very smooth hydrogen profile (solid line in Fig. 30.11a). The corresponding gradients are schematically sketched in Fig. 30.11b. The solid line is the decisive gradient of the Ledoux criterion. The region is fully convective in the innermost part, because $\nabla_{ad} < \nabla_{rad}$ and $\nabla_\mu = 0$. Next follows a radiative zone because of the drop of ∇_{rad}, above which a semiconvective layer exists, which would be convective according to the Schwarzschild criterion, but is stabilized due to the positive ∇_μ-term. If the mixing in the semiconvective region were very efficient, we would obtain a "plateau" in the profile (dashed line in Fig. 30.11a). There are obviously two main effects of such a mixing on the gradients. Firstly, any change of profile changes the value of ∇_μ, which goes to zero in the plateau. Secondly, the mixing increases the hydrogen content X_H in the lower part and decreases X_H in the upper part of the mixed region. In massive main-sequence stars the opacity is largely dominated by

electron scattering, for which $\kappa \sim (1+X_{\rm H})$, [cf. (17.2)]. Since $\nabla_{\rm rad} \sim \kappa$, [cf. (5.28)], the radiative gradient $\nabla_{\rm rad}$ is increased in the lower part and decreased in the upper part of the mixed area. Therefore both these changes (of ∇_μ and of $\nabla_{\rm rad}$), which are due to the mixing, will modify the decisive terms entering into (30.10), and as a result some parts can completely change their stability properties (convective-semiconvective-radiative). Whether a semiconvective layer becomes more stable or unstable to convection depends on the overall result of both effects. In the situation sketched, most likely the lower part, in which hydrogen content increases, will become fully convective, while the radiative envelope will grow deeper into the formerly semiconvective layer.

The slow mixing in semiconvective regions can be considered as a diffusion process (see, for instance, Langer et al. 1985). The resulting profile will depend on the timescale $\tau_{\rm diff}$ of that kind of diffusion and its ratio to the typical timescale in which the stellar properties change (e.g. the composition due to nuclear reactions). For example, a relatively small $\tau_{\rm diff}$ (large diffusion coefficient) will tend to mix to such an extent that convective neutrality is nearly reached with $\nabla_{\rm rad} \approx \nabla_{\rm ad}$. In fact this is yet another approach to treat semiconvection in numerical calculations: Semiconvective layers are mixed to such an extent that neutrality is achieved. In this case one does not aim at describing the physical properties in detail but rather aims at a likely final situation. In general one should expect a continuous change of the profile and radiative, semiconvective, and fully convective regions moving slowly through the star. Unfortunately the coefficient of diffusion cannot yet be determined satisfactorily, which is rather serious, since, as in the case of overshooting, the details of the established profile are very decisive for the later evolution of these stars. In Fig. 30.12 we show an example for the different convective and semiconvective layers establishing in a 15 $M_\odot$ star during the main-sequence evolution, when different approaches to overshooting and semiconvection are employed. The semiconvective layers outside the fully convective core in the Schwarzschild case (top panel in the figure) change their character–convective or radiative–with time, depending on changes in the thermal structure and on mixing. The result is a typical tongue-like extent of convective layers, separated by radiative "tongues", and a H/He profile that shows many irregular steps. This kind of structure can already be seen in the early works Langer (1989, 1991) in stars of 30 and 20 $M_\odot$.

Additional complications can arise from the interaction of semiconvection and overshooting. Note that semiconvection can also play a role in later phases, for example, if a convective core increases during helium burning and expands into a region of different chemical composition.

30.5 The Schönberg–Chandrasekhar Limit

Since the nuclear timescale for central hydrogen burning is large compared to the Kelvin–Helmholtz timescale, stars can be well represented by models in complete equilibrium throughout this phase. The question is now whether this continues to

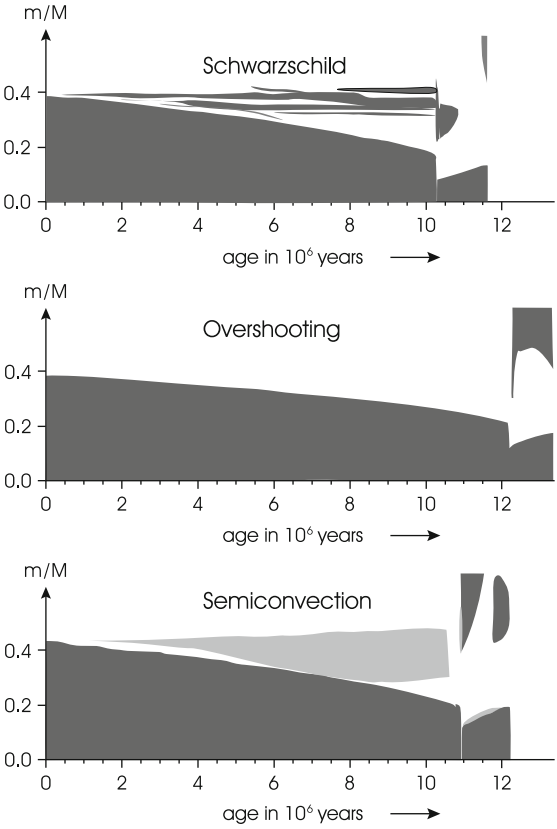

Fig. 30.12. Convective and semiconvective regions in a star of 15 $M_\odot$ for three different treatments of convection. The *top figure* shows fully convective regions (*dark grey*) if the Schwarzschild criterion is applied. The *bottom panel* shows the result if the Ledoux criterion is used, and slow semiconvective mixing is done according to the diffusive approach by Langer et al. (1985; with the free parameter in this description set to 0.1). Semiconvective regions are indicated by *light grey*. The *central panel* finally shows the case with overshooting considered as a diffusive process according to (30.9), with $f_{\rm ov} = 0.02$. Note that only the convective core ($\nabla_{\rm rad} \geq \nabla_{\rm ad}$) is shown; the region of overshooting, which extends over more than 5 % of the mass, is not visible in this figure (but see Fig. 30.10)

be valid also for the subsequent evolution. At the end of central hydrogen burning, the star is left with a helium core without nuclear energy release surrounded by a hydrogen-rich envelope. At the bottom of this envelope, the temperature is just large enough for further hydrogen burning, which continues at this place in a *shell source* (see Figs. 30.2 and 30.4). The problematic part is the possible structure and change of the helium core. A core almost in thermal equilibrium without nuclear energy sources cannot have a considerable luminosity, and hence must be nearly isothermal, since $dT/dr \sim l$.

Therefore we consider here equilibrium models consisting of an isothermal helium core of mass $M_{\rm c} = q_0 M$ and a hydrogen-rich envelope of mass $(1 - q_0)M$ (see Fig. 30.13). For simplicity the chemical composition is taken to change discontinuously at the border of the two regions. The luminosity is supplied by hydrogen-shell burning at the bottom of the envelope. In the following, solutions for the core (subscript 0 at its surface $q = q_0$) and solutions for the envelope (subscript e at the lower boundary $q = q_0$) are first discussed separately and then fitted to each other. In view of their importance we will look at the surprising results from different points of view.

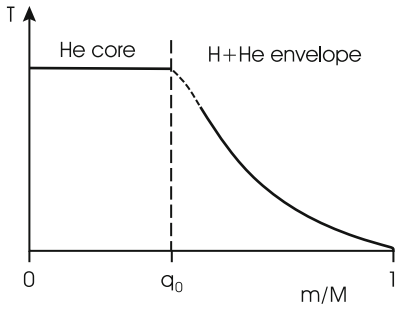

Fig. 30.13. Schematic temperature profile in an equilibrium model having an isothermal helium core of mass $q_0 M$. Hydrogen burns in a shell source at the bottom of the envelope, indicated by the *dashed part* of the line

30.5.1 A Simple Approach: The Virial Theorem and Homology

Important properties of such models can be understood by rather simple considerations, which give at least a qualitatively correct picture. We assume the isothermal core after central hydrogen burning to consist of an ideal monatomic gas (molecular weight $\mu_{\rm core}$). To this core, we apply the virial theorem in the form (3.21) which contains a term for the non-vanishing surface pressure P_0. Solving for P_0, we obtained (26.23), which we here rewrite as

$$P_0 = C_1 \frac{M_{\rm c} T_0}{R_{\rm c}^3} - C_2 \frac{M_{\rm c}^2}{R_{\rm c}^4}, \tag{30.11}$$

where C_1, C_2 are positive factors, and $C_1 \sim c_v = 3\Re/(2\mu_{\rm core})$. This describes the resulting surface pressure P_0 as the difference between the average interior pressure (first term $\sim \bar{\varrho} T_0$) and the self-gravity term (second term $\sim R_{\rm c} \bar{g} \bar{\varrho}$), when we use $\bar{\varrho} \sim M_{\rm c}/R_{\rm c}^3$ and $\bar{g} \sim M_{\rm c}/R_{\rm c}^2$.

For simplicity we assume $T_{\rm e}$ to be kept at a constant value by the thermostatic action of hydrogen burning. The fitting condition at q_0 then requires

$$T_0 = T_{\rm e} = \text{constant}, \tag{30.12}$$

and P_0 depends only on $M_{\rm c}$ and $R_{\rm c}$. As explained in Sect. 26.2 the counteraction of the two terms in (30.11), which depend on different powers of $R_{\rm c}$, has the result that, for $M_{\rm c} = \text{constant}$, P_0 has a *maximum value* $P_{0\,\rm max}$ at $R_{\rm c} = R_{\rm cmax}$ [see (26.27)],

$$R_{\rm cmax} = C_3 \frac{M_{\rm c}}{T_0}, \quad P_{0\rm max} = C_4 \frac{T_0^4}{M_{\rm c}^2}, \tag{30.13}$$

with some positive constants C_3, C_4. This can be obtained by solving $\partial P_0/\partial R_{\rm c} = 0$ (for constant T_0) from (30.11). The function $P_0(R_{\rm c})$ for given $M_{\rm c}$ and T_0 is sketched in Fig. 30.14. From (30.13) we see that $P_{0\rm max} \sim M_{\rm c}^{-2}$, i.e. the *maximum surface pressure of the core decreases strongly with the mass $M_{\rm c}$ of the core.*

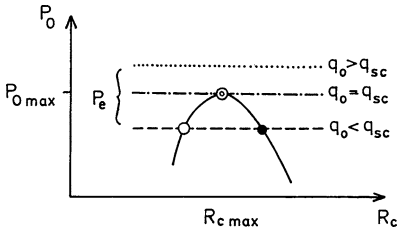

Fig. 30.14. The *solid line* shows schematically the pressure P_0 at the surface of the isothermal core as a function of the core radius R_c. *Horizontal lines* indicate the pressure P_c at the bottom of the envelope for three different relative core masses q_0. The stable solution is marked by a *dot* and the unstable solution by an *open circle*; the solution at P_{0max}, is marginally stable

For the functions at the bottom of the envelope we simply assume that all possible envelopes are homologous to each other. Then from (20.9) and (20.24) follow $P_e \sim M^2/R^4$ and $T_e \sim M/R$. The latter relation together with (30.12) means that M/R = constant, such that the relation for P_e becomes

$$P_e = C_5 \frac{T_0^4}{M^2}. \tag{30.14}$$

We see that P_e is independent of R_c and has the same dependence on T_0 as P_{0max}, but decreases with M instead of M_c. This can lead to difficulties! In Fig. 30.14 the envelope pressure P_e according to (30.14) is given by a horizontal straight line, the height of which depends on M.

The remaining fitting conditions for a complete solution of the star require $R_c = r_e$ and $P_0 = P_e$, i.e. we look for an intersection of the two types of curves in Fig. 30.14. Obviously this can be obtained only if $P_e \le P_{0max}$, which together with (30.13) and (30.14) gives the condition

$$q_0 \equiv \frac{M_c}{M} \le q_{SC}, \tag{30.15}$$

i.e. the *relative* core mass q_0 must not exceed a certain limiting value, which is the *Schönberg–Chandrasekhar limit* q_{SC}. This limit was already derived in Sect. 21.4 from fitting solutions for isothermal cores and for envelopes in the U–V plane.

For $q_0 < q_{SC}$ we have $P_e < P_{0max}$, and there are two intersections in Fig. 30.14. The solution for the smaller value of R_c is thermally unstable, the other one is stable. This can be made plausible by a simple argument. Figure 30.14 shows that, if we slightly increase the core radius of the stable solution, P_0 drops below P_e and the envelope tends to compress the core, thus restoring the equilibrium state. The opposite behaviour (further increase of an initial expansion, since P_0 exceeds P_e) can be seen to result from the perturbation of the unstable equilibrium state, and this rough argument is confirmed by a strict eigenvalue analysis.

The solutions merge for $q_0 = q_{SC}$ ($P_e = P_{0max}$) which corresponds to neutral stability. And there are no solutions possible for $q_0 > q_{SC}$, since P_e always exceeds P_0. In such a case some basic assumption of our present picture has to be dropped (e.g. equilibrium or ideal gas). In particular the Schönberg–Chandrasekhar limit does not apply for the case of a degenerate electron gas. This will be discussed later.

The value of q_{SC} has been computed by Schönberg and Chandrasekhar (1942). It depends on the ratio of the molecular weights μ_{core}/μ_{env}, since the envelope pressure depends on μ_{env}, while P_0 depends on μ_{core} via C_1. One can write roughly

$$q_{SC} = 0.37 \left(\frac{\mu_{env}}{\mu_{core}} \right)^2, \tag{30.16}$$

which means for a pure helium core $\mu_{core} = 4/3$ and for a hydrogen-rich envelope $q_{SC} \approx 0.09$. This value is certainly exceeded by the helium cores that are left after central hydrogen burning in stars of the upper main sequence. Stars of somewhat smaller mass may encounter the same difficulty later, when the shell source burns outwards, thus increasing the mass of the helium core above the critical value. The Schönberg–Chandrasekhar limit is therefore quite relevant for the evolution in any phases in which at a first glance one would expect isothermal cores of ideal gas to appear.

30.5.2 Integrations for Core and Envelope

More reliable curves in the $P - R_c$ diagram (Fig. 30.14) can be easily obtained by numerical integrations for core and envelope (Roth 1973).

An envelope solution can be calculated for given M and M_c by requiring the lower boundary conditions $l = 0, r = R_0$ to hold at $M = M_c$. The solution gives P_e and T_e at $m = M_c$. By varying R_c, one obtains a set of solutions which gives $P_e(R_c), T_e(R_c)$. Two typical envelope curves $P_e(R_c)$ are shown in Fig. 30.15a. It turns out that these curves, in their important parts, are nearly independent of M_c but are raised essentially by a decrease of M [This is qualitatively the same as in the approximation (30.14).]. The temperature T_e varies, in fact, very little along such an envelope curve. For later applications (Sect. 31.1) we briefly mention the surface values of these envelope solutions. Those with large values of R_c are located near the main-sequence. With decreasing R_c they move to the right in the HR diagram, and envelopes with the smallest values of R_c are close to the Hayashi line.

The solution for an isothermal core with temperature T_0 can be obtained by a straightforward integration starting at the centre with an assumed value of $P = P_c$ and continued until $m = M_c$ is reached. At this point one finds a pair of values $P = P_0$ and $r = R_c$. Many such integrations for different values of the parameter P_c then give the curve $P_0(R_c)$ for the core. The solid line in Fig. 30.15b gives such a curve for cores of mass $M_c = 0.18 M_\odot$ and $T_0 = 2.24 \times 10^7$ K. The lower-right part (small P_0, large R_c) corresponds to small central pressures P_c. With increasing

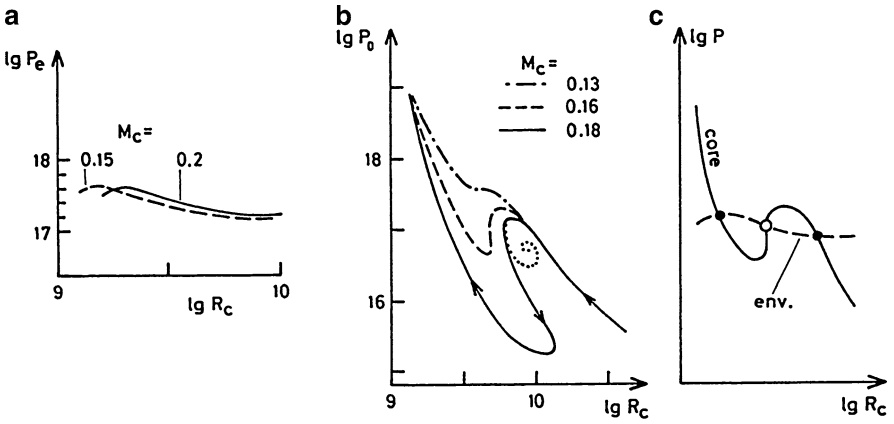

Fig. 30.15. Some typical curves of the pressure P (in dyn cm^{-2}) against the core radius R_c (in cm). (**a**) The pressure P_e at the lower boundary of the envelope for a stellar mass $M = 2M_\odot$ and two values of the core mass M_c (in $M_\odot$). (**b**) The pressure P_0 at the surface of isothermal cores of different mass M_c (in $M_\odot$). The *arrows* along the *solid curve* indicate the direction of increasing central pressure. The *dotted spiral* is with neglect of degeneracy. (**c**) Sketch of core and envelope curves for the case of three intersections giving three complete solutions (*filled circles* stable, *open circle* unstable) (After Roth 1973)

P_c the curve leads up to the maximum and decreases again (This corresponds to the maximum of the core curve in Fig. 30.14, while the horizontal envelope curves there are now replaced by envelope curves like those in Fig. 30.15a.). Then it would follow the dotted spiral, if we artificially suppress the deviation from the ideal-gas approximation in the equation of state. This may be compared with the spiral in the U–V plane obtained for an isothermal core in Fig. 21.2. An increasing P_c, however, implies an increasing degeneracy of the electron gas. This "unwinds" the spiral and P_0 drops, while a gradually increasing fraction of the core becomes degenerate. When degeneracy encompasses practically the whole core, P_0 rises again strongly with decreasing R_c (upper-left end of the solid curve in Fig. 30.15b). The dashed and dot-dashed lines demonstrate how the curve changes when M_c is decreased. As predicted by (30.13) the maximum shifts to smaller R_c and larger P_0. The main effect, however, is that the minimum is less and less pronounced. This goes so far that finally the maximum, which is decisive for the existence of a Schönberg–Chandrasekhar limit, has disappeared. A similar change of the structure of the curve is obtained if, instead of decreasing M_c, we increase the temperature T_0.

30.5.3 Complete Solutions for Stars with Isothermal Cores

As mentioned, each sequence of envelope solutions yields a relation $T_e = T_e(R_c)$. Assume now that along a corresponding sequence of isothermal-core solutions

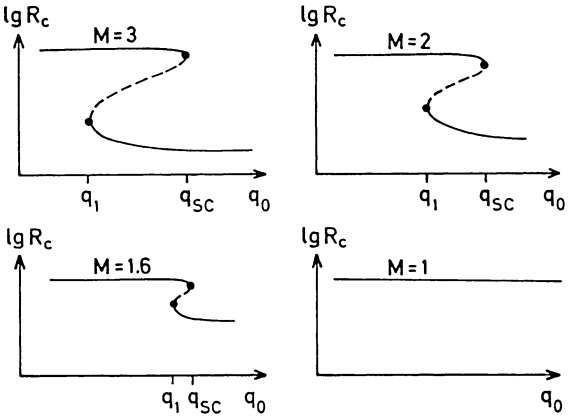

Fig. 30.16. Complete equilibrium solutions for four different stellar masses M (in $M_\odot$) having an isothermal core of mass $M_c = q_0 M$. Each solution here is characterized by its core radius R_c and its relative core mass q_0. Branches with thermally stable solutions are shown by *solid lines* and branches with unstable solutions by *dashed lines*. The turning point at $q_0 = q_{SC}$ defines the Schönberg–Chandrasekhar limit (After Roth 1973)

T_0 is varied such that $T_0(R_c) = T_e(R_c)$ for all R_c. This deforms a core curve in Fig. 30.15b only slightly. Any intersection of this new core curve with a corresponding envelope curve gives a complete solution, since we then have at $m = M_c$

$$r_e = R_c, \quad P_e = P_0, \quad T_e = T_0, \quad l_e = l_0 = 0, \tag{30.17}$$

i.e. continuity of all variables.

Suppose that the core curve has a pronounced maximum. We can then obviously expect to have up to three solutions (see Fig. 30.15c), one with an ideal gas (largest R_c), the second with partial degeneracy (intermediate R_c), and the third with large degeneracy (smallest R_c) in the core. If the envelope curve passes below the minimum or above the maximum of the core curve, there will be only one solution. And there can also be only one solution with a monotonic core curve.

The resulting solutions for different values of M and M_c can best be reviewed by representing them as models in which $q_0 = M_c/M$ varies as a parameter while M is fixed (Fig. 30.16). Each model is represented here by its core radius R_c in order to give an easy connection with the foregoing fitting procedure.

Figure 30.16 shows that for larger M the sequence of equilibrium solutions consists of three branches. Two of them contain thermally stable models (solid lines), the other unstable models (dashed). On the upper and lower stable branches, the isothermal cores have no or strong degeneracy respectively. The branches are connected by two turning points (at q_1, and q_{SC}) where the models have marginal stability. A real star would first evolve along the upper stable branch, increasing its core at nearly constant radius. When the mass of the core reaches the turning point, the core will contract on a thermal timescale (q_0 staying constant because of

the much longer nuclear timescale) to the lower branch. The turning point with the larger q_0 defines the Schönberg–Chandrasekhar limit. Its value q_{SC} turns out to be nearly independent of M. For $q_1 < q_0 < q_{SC}$, there are three solutions, otherwise one solution. When going to gradually smaller M, we see that q_1 approaches q_{SC}, until both turning points merge and finally disappear for $M < 1.4M_\odot$. For such small M, therefore, one has only one (stable) branch and no Schönberg–Chandrasekhar limit. This agrees with what one expects from the core curves given in Fig. 30.15b. It shows, for example, that the curves are already monotonic for $M = 1.3M_\odot$ and $q_0 \leq 0.1$ (i.e. $M_c \leq 0.13M_\odot$) (The exact mass values depend not only on the chemical composition, but also on the detailed physical input of the stellar models. Those given here are from the model calculations by Roth 1973, but are representative.). Instead of R_c, we might have plotted the stellar radius R over the parameter q_0. As mentioned above, small R_c corresponds to large R and vice versa. The sequences for large enough M would then exhibit a stable dwarf branch for $q_0 < q_{SC}$, a stable giant branch for $q_0 > q_{SC}$ and an unstable intermediate branch.

In evolutionary models one will encounter a smooth profile rather than a discontinuity of the chemical composition. In such a case various definitions of the core mass are possible: it can be the point at which $X_H > 0$, or where the maximum of shell source burning is located. Since the shell is comparably thin, the various definitions do not differ too much from each other, anyhow. The Schönberg–Chandrasekhar limit can be identified by the departure from thermal stability, i.e. by a higher fraction of thermal to nuclear energy. In any case, one finds again that $q_{SC} \approx 0.1$.